SANDIA REPORT
SAND2014-15546
Unlimited Release
Printed June 2014

Identified Corrosion and Erosion Mechanisms in SCO2 Brayton Cycles

Darryn Fleming, SNL/NM, and Alan Kruizenga, SNL/CA

Prepared by
Sandia National Laboratories
Albuquerque, New Mexico 87185 and Livermore, California 94550

Sandia National Laboratories is a multi-program laboratory managed and operated by Sandia Corporation, a wholly owned subsidiary of Lockheed Martin Corporation, for the U.S. Department of Energy's National Nuclear Security Administration under contract DE-AC04-94AL85000.

Issued by Sandia National Laboratories, operated for the United States Department of Energy by Sandia Corporation.

Available to DOE and DOE contractors from
U.S. Department of Energy
Office of Scientific and Technical Information
P.O. Box 62
Oak Ridge, TN 37831

Telephone: (865) 576-8401
Facsimile: (865) 576-5728
E-Mail: reports@adonis.osti.gov
Online ordering: http://www.osti.gov/bridge

Available to the public from
U.S. Department of Commerce
National Technical Information Service
5285 Port Royal Rd.
Springfield, VA 22161

Telephone: (800) 553-6847
Facsimile: (703) 605-6900
E-Mail: orders@ntis.fedworld.gov
Online order: http://www.ntis.gov/help/ordermethods.asp?loc=7-4-0#online

Identified Corrosion and Erosion Mechanisms in SCO2 Brayton Cycles

Darryn Fleming, SNL/NM
and
Alan Kruizenga, SNL/CA

Prepared by
Sandia National Laboratories
Albuquerque, NM 87185

Executive Summary

Supercritical Carbon Dioxide (S-CO2) is an efficient and flexible working fluid for power production. Research to interface S-CO2 systems with nuclear, thermal solar, and fossil energy sources is currently underway. To proceed, we must address concerns regarding compatibility of materials, at high temperature, and compatibility between significantly different heat transfer fluids.

Dry, pure S-CO2 is thought to be relatively inert [1], while the addition of ppm levels of water and oxygen result in formation of a protective chromia layer and iron oxide [2]. Thin oxides are favorable as diffusion barriers, and for their minimal impact on heat transfer. While S-CO2 is typically understood to be the secondary fluid, many varieties of primary fluids exist for nuclear applications. Molten salts, for use in the Molten Salt Reactor concept, are given as an example to contrast the materials requirements of primary and secondary fluids. Thin chromia layers are soluble in molten salt systems (nitrate, chloride, and fluoride based salts) [3-8], making materials selection for heat exchangers a precarious balancing act between high temperature oxidation (S-CO2) and metal dissolution (salt side of heat exchanger).

Because concerns have been raised regarding component lifetimes, S-CO2 work has begun to characterize starting materials and to establish a baseline by analysis of 1) as-received stainless steel piping, and 2) piping exposed to S-CO2 under typical operating conditions with Sandia National Laboratories' Brayton systems.

A second issue discovered by SNL involves substantial erosion in the turbine blade and inlet nozzle. It is believed that this is caused by small particulates that originate from different materials around the loop that are entrained by the S-CO2 to the nozzle, where they impact the inlet nozzle vanes, causing erosion. We believe that, in some way, this is linked to the purity of the S-CO2, the corrosion contaminants, and the metal particulates that are present in the loop and its components.

Contents

Contents 5
Figures 6
Tables 7
Nomenclature 7
1. Introduction 10
2. Heat Exchanger Material Concerns For S-CO2 11
2.1 Heat Exchanger Concepts 12
2.2 Materials for use with Halide-Based Molten Salts 13
2.3 Materials for S-CO2 Systems 14
2.4 Path Forward for Heat Exchanger Materials 16
3. GEN IV RCBC Materials Analysis 23
3.1 316L Pipe Analysis 23
3.2 Turbine Erosion 24
3.3 Nozzle Erosion 25
3.4 Discussion of Particulate Source 25
3.5 Conclusion and Path Forward 26
Tables 30
References 31

Figures

Figure 1: Cycle efficiency as a function of temperature for several types of power conversion systems. Thermodynamic calculation indicates that CO2 has the greatest efficiency gains at temperatures of 500-600°C. 17
Figure 2: H2X concept showing diffusion bonded structure[18]. Small semi-circular channels would allow flow of the S-CO2, where large, plate-formed channels would be used for molten salt, or possibly liquid sodium. 17
Figure 3: Nickel strike was used to protect surfaces during the diffusion bonding process. X-ray maps the diffusion bond, shown here, between layers of 316L stacked plates which indicate a change in weld chemistry, relative to the base alloy, due to the nickel strike..... 18
Figure 4: Ellingham diagram of oxides for common alloying constituents for high-temperature alloys [30]. More negative values are indicative of increased thermodynamic stability. As many transition elements (e.g., Cr, W, Mo) are soluble in nitrate melts, it may become necessary to employ materials or coating barriers that are thermodynamically stable relative to the melt. 19
Figure 5: Gibb's free energy for chloride (left) and fluoride (right) systems. Chromium halides are most thermodynamically favored, followed by iron halides, then nickel halides..... 19
Figure 6: X-ray map showing a cross section with relative concentration of Cr. Dark regions indicate preferential depletion (Alloy 617 in KCl-MgCl2) [6]..... 20
Figure 7: Thermodynamic comparisons of nitrates, oxides, and chromates. As chrome oxides are readily formed, due to thermodynamic stability relative to the nitrate salt, thus results in a reaction pathway from oxide to soluble chromate. 20
Figure 8: Metal loss after 3000 hours in a 60/40 nitrate salt [3] vs. soluble transition metals. Kinetics of corrosion is slow, as indicated by the low metal loss rate, but is proportional to transition metals. 21
Figure 9: Two SEM images of the in-service SS 316L piping showing significant intergranular corrosion and pitting. 27
Figure 10: Sample location in schematic view (red circle) (a). Sample location is within physical view (red circle) (b). Corrosion sample removed (c)..... 27
Figure 11: 100x (left) and 500x (right) images indicate surface features indicative of intergranular attack. Some surface scale was observed, and will be identified using electron spectroscopy techniques..... 28
Figure 12: Turbine nozzle (left) with substantial amount of erosion, and turbine wheel (right) with placement inside turbine nozzle..... 28
Figure 13: Compressor (left) and compressor diffuser (right) showing no signs of erosion. 28
Figure 14: Erosion on the Turbine (L); particulate erosion on turbine blade (R). 29
Figure 15: SEM showing different microstructure. 29
Figure 16: Turbine Nozzle with undercut; EDS sample location identified. 29
Figure 17: Layout during test (left) and modified layout after erosion (right). 29

Tables

Table 1: EDS comparison: IN C-22 vs. actual on turbine wheel 30
Table 2: EDS comparison: IN 718 vs. actual on turbine nozzle 30

Nomenclature

BEI	Backscatter Electron Imaging
°C	Degrees Centigrade
CO2	Carbon Dioxide
CSP	Concentrated Solar Power
DB	Diffusion Bond
DOE-NE	U.S. Department of Energy – Office of Nuclear Energy
EDS	Energy Dispersive Spectroscopy
FLiBe	Lithium-Beryllium Fluoride Salt
FM	Ferritic-Martensitic
GEN IV	Generation IV
HTF	Heat Transfer Fluid
HX	Heat Exchanger
H^2X	Hybrid Heat Exchangers
IA	Intergranular Attack
IN	Inconel
MSR	Molten Salt Reactor
Ni	Nickel
PCHE	Printed Circuit Heat Exchanger
RCBC	Recompression Closed Loop Brayton Cycle
SEM	Scanning Electron Microscopy
S-CO2	Supercritical Carbon Dioxide
SGS	Steam Generation System
SNL	Sandia National Laboratories
SS	Stainless Steel
TAC	Turbine Alternator Compressor
TES	Thermal Energy Storage
μm	Micrometer
XS	Cross-sectional

Nominal Alloy Compositions (weight percent basis)*

Al-6XN	Fe-24Ni-21Cr-6Mo
HA230	Ni-22Cr-14W-5Co-3Fe-2Mo
HA 242	Ni-24Mo-7Cr-2.5Co-2Fe
In625	Ni-22Cr-9Mo-4Cb+Ta-3Fe
PE16	Ni-34Fe-17Cr-3Mo-1Al-1Ti
T91	Fe-9Cr
310SS	Fe-25Cr-22Ni-2Mn-1Si
316SS	Fe-17Cr-12Ni-3Mo-2Mn-1Si
800H	Fe-32Ni-21Cr-2Mn-1Si

*Constituents less than 1% not included

1. Introduction

The Supercritical Carbon Dioxide (S-CO2) Recompression Brayton Cycle (RCBC) is being investigated at Sandia National Laboratories (SNL). The Department of Energy, Office of Nuclear Energy (DOE-NE), has successfully completed the construction of the 1 MWth S-CO2 RCBC testing platform, and testing is underway [2]. As more hours of operation are applied to the RCBC power loop, uncertainty in the long-term reliability of various components has become more visible. More testing and analysis should be done to complete a rigorous assessment.

Preventive maintenance practices are utilized at SNL to avoid untimely failures [3]. Practices such as periodic bore scope inspection and time-lapsed comparison of components and piping are employed. Recently, as part of this effort, Sandia extracted the piping used in the RCBC through September 2012, and subjected it to standard metallurgical analyses: optical microscopy, scanning electron microscopy (SEM), and energy dispersive spectroscopy (EDS).

Ultimately, Sandia established a program to actively monitor the corrosion characteristics of components from the start of service to the end of service lifetime. Results to date have demonstrated the need for this investigative program. For example, during visual turbomachinery inspections, it was noted that the turbine nozzles appeared eroded, with no precise root cause identified. The nozzles had suffered severe erosion, which resulted in geometrical changes that were visually observed. The turbine also showed visual evidence of wear, but this wear was often ignored because the actual "life span" of the turbine was so unpredictable. The nozzle and turbine components were ultimately removed from service and analyzed with microscopy. Materials issues are of concern, given the following reasons 1) the solvent nature of S-CO2 [4], and 2) its ability to transport small, dissolved particles throughout the loop, the combination of which causes erosion at high gas-velocity locations, such as the turbine inlet.

This report is divided into two distinct sections. Section one provides an overview of corrosion mechanisms in S-CO2, and in molten salts for nuclear applications, with a focus on competing mechanisms for heat exchangers. Section two presents the materials issues and analysis from the RCBC at SNL.

2. Heat Exchanger Material Concerns For S-CO2

Historically, the optimization of Rankine power cycles yielded modest improvements through balance-of-plant activities, such as heat/re-heat processes and improving system components. Efficiency improvements to this power cycle are yielding asymptotic return on investment, so new cycles are being explored

Traditionally the Rankine cycle, operating with steam, utilizes a turbine connected to a generator to produce electricity. The Rankine cycle is popular, thanks to many years of use and experience. Calculated Carnot efficiencies dictate that an increase in the upper temperature limit benefits system performance, assuming that the heat rejection temperature is constant. This drives current research toward higher temperatures.

Fluids have been suggested and adopted to meet the goal of increased system efficiency. Supercritical fluids (SCF), that is, fluids at pressures above their critical pressure, reduce cycle complexity by avoiding phase change and two-phase behavior. Experiments have begun to use SCFs in Brayton cycles that operate at higher temperatures, rather than Rankine cycles, thanks to their theoretically superior efficiency. Figure 1 shows the expected increase in efficiency when using SCFs in Brayton cycles.

Water was an early SCF candidate due to the extensive operating knowledge gained from years of using water with Rankine cycles. However, supercritical water is extremely corrosive, making it difficult to use in the turbines and compressors present in a Brayton cycle.

To avoid water's corrosive effects, supercritical carbon dioxide (S-CO2) was investigated as the working fluid in a Brayton configuration, and was found to be favorable from an efficiency standpoint [9, 10]. Given the corrosive behavior of water, supercritical carbon dioxide (S-CO2) is under evaluation as a working fluid in Brayton cycles, and, in results to date, has appeared efficient. Research on S-CO2 in Brayton cycles is led by the Advanced Nuclear Concepts group at Sandia National Laboratories. This group conducted extensive experiments with S-CO2 and its effect on turbomachinery, bearings, seals, and other assorted component and technology options for Brayton cycles.

In the context of nuclear power conversion systems, S-CO2 lends itself to serving as either a primary or a secondary coolant. Direct cycle gas reactor configurations that utilize S-CO2 as a primary coolant exhibit improved heat transfer characteristics compared to other gas coolants, such as helium. These configurations using S-CO2 may also better mitigate accidents than other available coolants.

As a secondary coolant coupled to the primary coolants of light-water, heavy-water, molten salt, or liquid metal cooled reactors, S-CO2 provides superior heat transfer characteristics, and can improve system efficiency up to 50%. While nuclear applications have spearheaded S-CO2 efforts through the past decade, recent research recommends considering this cycle for solar and fossil applications [11-13].

One of the near-term deployment opportunities for the S-CO2 Brayton is thought to be in concentrated solar power (CSP) plants [14], due to the need to reduce costs. State-of-the-art CSP plants use a binary salt, a mixture of sodium nitrate and potassium nitrate. This technology parallels the challenges that would need to be overcome in nuclear systems utilizing halide-based salts, such as the lithium-beryllium-fluoride (FLiBe) systems or lithium-sodium-potassium fluoride (FLiNaK) systems. The key interfaces between the primary and secondary coolant systems are the heat exchangers.

Current molten salt systems, used in CSP plants, employ U-tube exchangers as the steam generator. These steam generation systems (SGS) operate at temperatures below 600°C and have been able to utilize 300-series stainless steels. Nuclear molten salts, likely halide based (i.e., chloride or fluoride), will require materials selected specifically for their use at higher temperatures and having lower concentrations of chromium, such as Haynes 242 [4], which has significant additions of molybdenum.

This section discusses materials selections for heat exchangers that incorporate, for illustration purposes, a halide-based molten salt and S-CO2 systems. A brief discussion of molten salt corrosion mechanisms is summarized with pertinent thermodynamic calculations, as is S-CO2 material performance. Issues related to heat exchangers are addressed, with recommendations for future heat exchanger development.

2.1 Heat Exchanger Concepts

There are several heat exchanger (HX) concepts that couple S-CO2 systems to low pressure heat transfer fluids, such as molten salts or liquid metals. Two types are discussed here: shell-and-tube type and plate type.

Shell-and-tube heat exchangers have a historical precedent for heat transfers between a high-pressure and a low-pressure fluid. The high-pressure fluid is contained within the tube, while the shell contains the low-pressure fluid. A plethora of configurations, passes, and flow paths exist, all of which largely depend on the application. HX fabrication is laborious owing to the complex configuration of tubes, necessitating many welds. The comparatively high cost of labor is mitigated by the large body of knowledge on shell-and-tube HX. Thanks to familiarity, this configuration is in regular use in industry.

Plate-type HX include printed circuit heat exchangers (PCHE), which consist of chemically etched flow channels in metal plates that are diffusion bonded (DB) together. Hot and cold channels are stacked in alternating layers and have inlet manifolds at each plate end to distribute flows. PCHEs gained significant popularity thanks to their compact nature, produced by large UA values. This results in heat exchangers that are up to 85% smaller than shell-and-tube systems [15]. Because the hydraulic diameter is on the order of one millimeter [16], concerns about plugging of liquid sodium [17], or freezing events with molten salts, have slowed the adoption of PCHE. To mitigate plugging, engineers developed a modified plate HX called the Hybrid Heat Exchanger (H^2Xs) [18]. The design, similar to PCHE designs, consists of an alternating arrangement of etched channel plates that are diffusion bonded to fins on the parting sheet (Figure 2). In this design, S-CO2 flows through the PCHE, providing pressure

containment, while the molten salt or liquid metal flows through the finned structure. Larger diameters reduce the surface area to volume ratios, and lessen the risk for freezing or plugging.

Diffusion bonded heat exchangers are limited primarily by the widespread lack of diffusion bonding parameters, as much of this information is proprietary. Work is underway to understand and optimize the diffusion bond process through use of a 316L stainless steel stack consisting of 24 plates [13]. Results show excellent bond quality (Figure 3), with nickel enrichment along the bond interface. The diffusion process requires surfaces free from debris and surface oxides. The first series of tests employed nickel plating to prevent the surface oxidation that is detrimental in the diffusion bond.

Regardless of which concepts are utilized in the future, materials must be tailored to the fluid in question. Thermodynamic calculations, an understanding of kinetics, and operational experience are critical for making the appropriate material choices.

2.2 Materials for use with Halide-Based Molten Salts

Alloys used with high-temperature molten salts (above 500°C) degrade through two primary pathways: high-temperature oxidation/chlorination, and selective dissolution. High-temperature oxidation occurs through interaction between the halide anion (i.e., Cl^- or $F^{-)}$ and a high-temperature alloy (salt containment or exposed samples), which forms various species. Molten salts behave differently with regards to high-temperature oxidation. Under high-temperature oxidation, alloys are largely protected by the formation of stable barriers. Major classes include chromia (Cr_2O_3) and alumina formers (Al_2O_3). Thermodynamics provide a chemical roadmap toward the expected species present.

The products formed by high-temperature oxidation are determined by Ellingham diagrams, which assess the relative stability of compounds as a function of temperature. Ellingham diagrams will be a primary tool in understanding chemical behavior (the authors assume that readers have little prior knowledge of these behaviors).

Pure elements (i.e., metal Cr or O_2) have a Gibbs energy value of zero, thus serving as a reference point. It is known that under ambient conditions chromium and oxygen react to form chromia, leading to the "stainless" quality of high Cr-content alloys by acting as a kinetic barrier limiting the migration of oxygen into the base alloy [19]. Brushing aside any complexities due to kinetics, the following equation can be considered:

$$2Cr + \frac{3}{2}O_2 \overset{?}{\rightarrow} Cr_2O_3$$ **Equation 1**

The Gibbs free energy for chromia is then calculated by:

$$\Delta G^{\circ}_{Cr2O3} = \Delta H^{\circ} - T\Delta S^{\circ}$$ **Equation 2**

$$\Delta H^{\circ} = \sum nH^{\circ}_{f,products} - \sum mH^{\circ}_{f,reactants}$$ **Equation 3**

$$\Delta S^{\circ} = \sum nS^{\circ}_{f,products} - \sum mS^{\circ}_{f,reactants}$$ **Equation 4**

Assuming standard conditions (values for Gibbs free energy is tabulated by various parameters) the resulting value is ΔG°= -1158[kJ/mol].Values that are negative, as listed here, are favored thermodynamically, and would be expected, barring one major caveat: kinetic barriers are negligible for the conditions under consideration.

Figure 4 is an extension of the above example, but with the oxides of commonly used metals for alloying constituents (i.e., Ni, Fe, Cr, Mo, W, Co). As illustrated in Figure 4, for all temperatures listed, Cr2O3 is the thermodynamically favored oxide among all the species calculated. In practical application, this is frequently the case.

The Ellingham diagram can also be applied toward molten salt systems. Figure 5 shows that between Fe, Ni, and Cr, CrCl3 / CrF3 is favored by relative indication on the Ellingham diagram, and is analogous to Cr2O3 with one major difference: CrCl3 / CrF3 dissolves in molten salts. Practically speaking, no protective barrier can be formed and chromium is preferentially removed from alloys. Literature readily confirms this fact, with one such example shown in Figure 6 [6]. More comprehensive data are available for molten nitrate salts, where the soluble metals are primarily Cr, W, and Mo. This behavior is paralleled in molten nitrate salts, shown by the calculations in Figure 7. Figure 8 shows the correlation between the dissolution of soluble metals and corrosion rates [3].

Optimal heat exchanger performance depends upon minimizing corrosion. Primary fluids (molten salt, liquid metal, water, etc.) will all have unique materials compatibility requirements that will restrict heat exchanger design. The use of advanced heat exchanger geometries will require further research into the primary fluid of choice.

2.3 Materials for S-CO2 Systems

Corrosion considerations for S-CO2 are both similar and starkly different when compared to those for molten nitrates. High-temperature oxidation is a similar corrosion mechanism in both S-CO2 and salt systems. The difference is that, in the S-CO2 system, chromia oxides are stable, and no dissolution has been observed during operation of with pure CO_2 [2]. Another

consideration in alloy selection is the long term performance due to carburization, also called metal dusting.
High temperature oxidation thermodynamics, and ultimately corrosion rates, will be subject to the purity of the CO_2 used in the system. While less materials corrosion data is available for S-CO2 at high temperatures, a significant numbers of studies from the petroleum industry involving CO_2 and water have been performed with carbon steels. Carbon steels are commonly used as transportation pipelines for petroleum. Enhanced oil recovery has an application space where CO_2 is dissolved in water. Interaction with water and CO_2 will result in the formation of carbonic acid (H_2CO_3), which is called "sweet" corrosion. Formation of an acid enables half-cell redox reactions, as follows [20]:

$$Fe \rightarrow Fe^{2+} + 2e \qquad \textbf{Equation 5}$$
$$2H^{+} + 2e \rightarrow H_2 \qquad \textbf{Equation 6}$$

The iron cation will react with carbonate to form iron carbonate ($FeCO_3$). An increase in temperature will increase the corrosion rates in CO_2 systems [20]. Furthermore, corrosion rates are enhanced at increasing pressures, due to an ever-increasing solubility of water in CO_2, which directly correlates to concentrations of carbonic acid. Corrosion rates for alloy X65 (Fe-1.4Mn-0.28C), at 80°C, increased from 1.64mm/year to 7.26mm/year by raising the pressure from 1MPa to 9.1MPa [21]. No clear differences in mechanisms were apparent in sub-critical vs. supercritical pressures, only differences in rates. Therefore, minimizing and eliminating water from high temperature S-CO2 would reduce corrosion rates. Such principles from low-temperature work should influence work performed at high temperatures.

Research exists on high-temperature corrosion behavior for several families of alloys, specifically ferritic-martensitic (FM) steels and austenitic steels. FM steels, while less expensive than austenitic steels, exhibit corrosion rates one-to-two orders of magnitude higher than austenitic stainless steels in temperatures of 550-650°C [22, 23]. FM steels form duplex corrosion layers, where magnetite is the outermost corrosion layer in contact with S-CO2 and, beneath the magnetite, is a layer of spinel that extends to the base alloy [22, 23]. FM steels may be a viable option for lower temperatures. However, at temperatures of 550°C, a linear oxidation extrapolation to one year indicates alloy attack on the order of 416µm/year for a Fe-9Cr steel (T91)) [24].

By comparison, austenitic stainless steel exhibits much less corrosion. In one test, alloy 800H had 2-5µm of surface scale (650°C, 20.7MPa), while in the same test, T91 had 46-127 µm of oxide [23]. Performance of alloys differs by more than an order of magnitude in favor of the austenitic alloy. Studies to date have investigated the following austenitic and nickel based alloys for up to 3000 hours (650°C, ~20MPa); these alloys are presented in order of the best-to-worst performers based on approximate weight gain data (mg/cm^2): 800H ~ HA230 (0.15) < PE16 ~ In625 (0.17) < 310SS ~ Al-6XN (0.20) << 316SS (1.75) [23, 25, 26].

Carburization is another materials degradation concern in high temperature S-CO2 systems. Despite the formation of thick oxides present on FM steels, carburization was found on the base alloy at temperatures as low as 550°C [27]. Consequences of carburization are complex. First, if carbon uptake occurs too quickly, some of the carbon becomes trapped in the oxide scale, increasing porosity. Next, as carbon diffuses into the metal matrix, formation of chromium

carbides occurs, effectively sensitizing the steel and increasing susceptibility to stress corrosion cracking. Carburization information on austenitic and nickel-based stainless steels is incomplete. That said, at high temperatures, carbon activity may have detrimental effects in terms of the stability of chromium carbides, which may reduce the corrosion resistance of austenitic alloys.

2.4 Path Forward for Heat Exchanger Materials

There are many opportunities for impacting heat exchanger design for supercritical carbon dioxide Brayton cycles, specifically for high-temperature heat exchangers. Outstanding issues include heat exchanger geometries and materials, corrosion mechanisms associated with the primary coolant, and corrosion mechanisms associated with supercritical carbon dioxide.

Tailoring heat exchanger materials is a logical choice, making printed-circuit heat exchangers, or, more realistically, hybrid heat exchangers, attractive options. Diffusion bonding is frequently used for dissimilar metals [28, 29]. Determining optimal bonding parameters and fabrication procedures, and ensuring bond quality are difficult tasks. It is not enough to simply research this process; engineers must gain enough data to code qualify a product used in the field.

Materials for use with molten salts (as the primary coolant example given) and supercritical carbon dioxide require different chemistries, based on the heat transfer fluid's corrosion mechanisms. There is more information at present regarding high-temperature oxidation and best alloys for use with molten salts. However, there is limited information available regarding the effect of water in supercritical carbon dioxide systems, and the setting of practical limits of water within S-CO2 must be done. Additional research on high-temperature CO_2 is required for system design, especially in light of the carburization present.

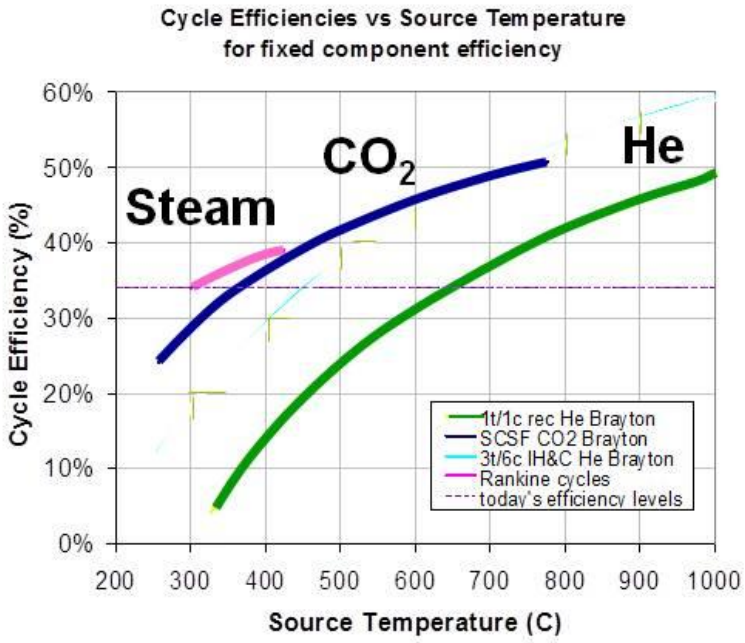

Figure 1: Cycle efficiency as a function of temperature for several types of power conversion systems. Thermodynamic calculation indicates that CO2 has the greatest efficiency gains at temperatures of 500-600°C.

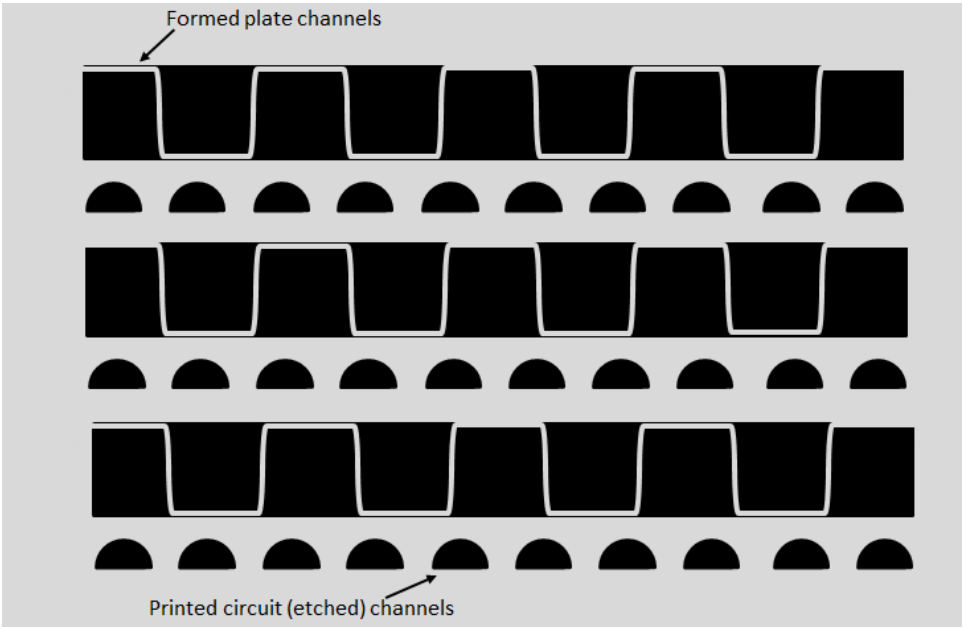

Figure 2: H^2X concept showing diffusion bonded structure[18]. Small semi-circular channels would allow flow of the S-CO2, where large, plate-formed channels would be used for molten salt, or possibly liquid sodium.

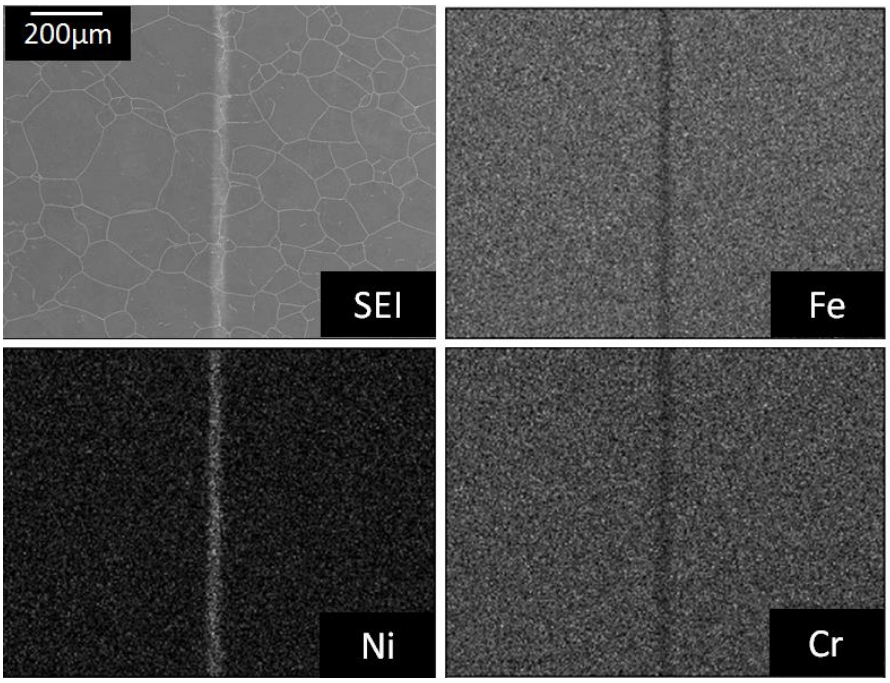

Figure 3: Nickel strike was used to protect surfaces during the diffusion bonding process. X-ray maps the diffusion bond, shown here, between layers of 316L stacked plates which indicate a change in weld chemistry, relative to the base alloy, due to the nickel strike.

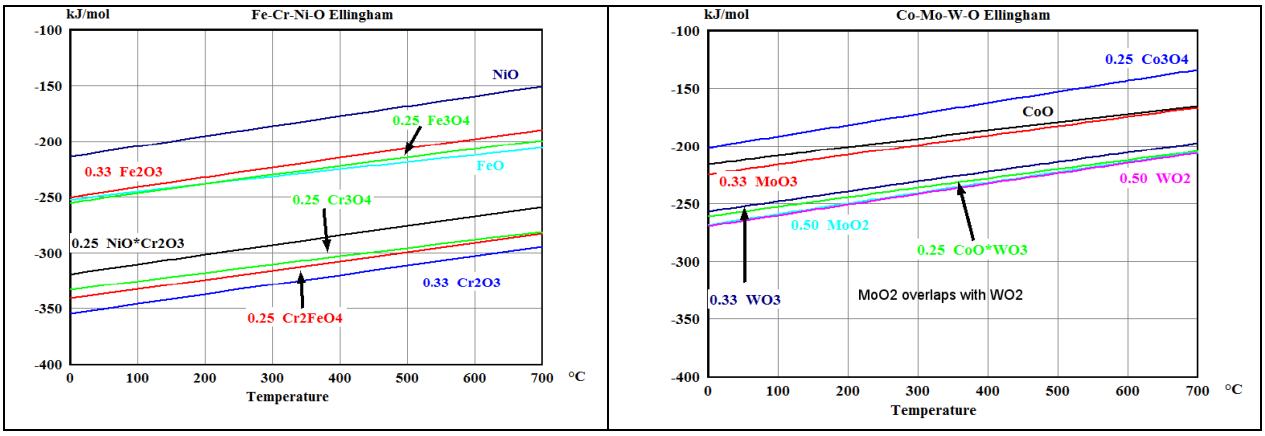

Figure 4: Ellingham diagram of oxides for common alloying constituents for high-temperature alloys [30]. More negative values are indicative of increased thermodynamic stability. As many transition elements (e.g., Cr, W, Mo) are soluble in nitrate melts, it may become necessary to employ materials or coating barriers that are thermodynamically stable relative to the melt.

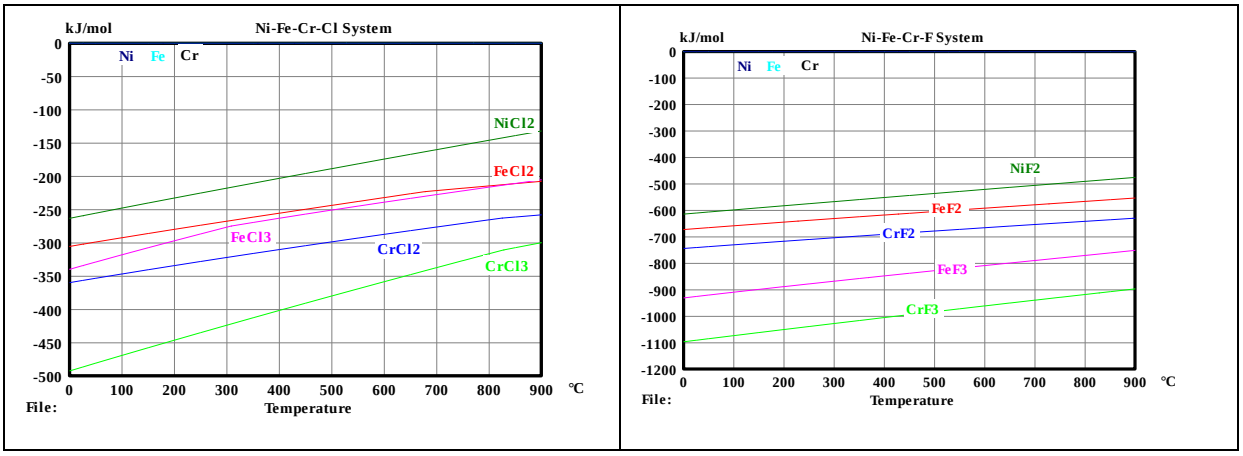

Figure 5: Gibb's free energy for chloride (left) and fluoride (right) systems. Chromium halides are most thermodynamically favored, followed by iron halides, then nickel halides.

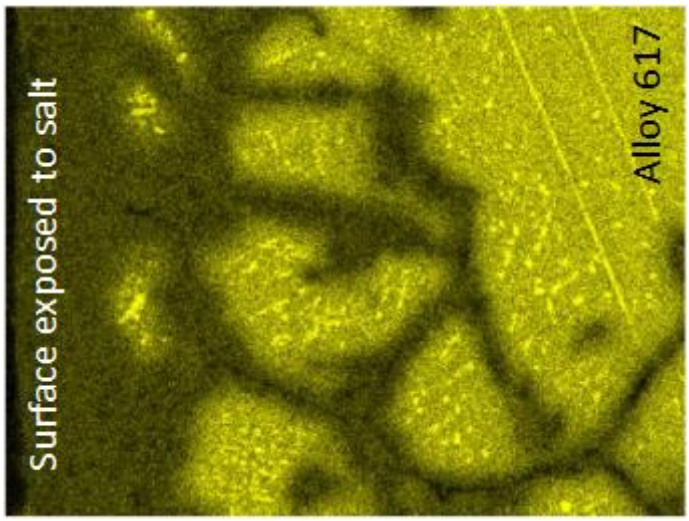

Figure 6: X-ray map showing a cross section with relative concentration of Cr. Dark regions indicate preferential depletion (Alloy 617 in KCl-$MgCl_2$) [6].

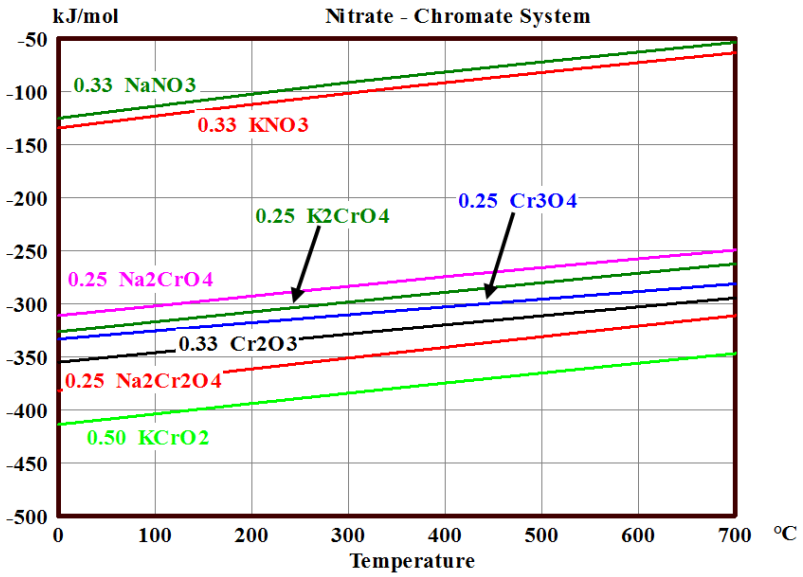

Figure 7: Thermodynamic comparisons of nitrates, oxides, and chromates. As chrome oxides are readily formed, due to thermodynamic stability relative to the nitrate salt, thus results in a reaction pathway from oxide to soluble chromate.

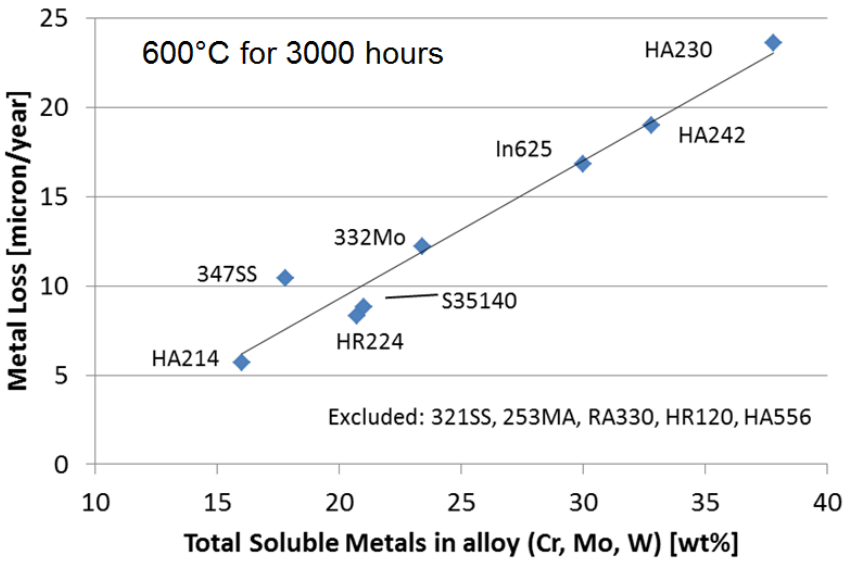

Figure 8: Metal loss after 3000 hours in a 60/40 nitrate salt [3] vs. soluble transition metals. Kinetics of corrosion is slow, as indicated by the low metal loss rate, but is proportional to transition metals.

3. GEN IV RCBC MATERIALS ANALYSIS

3.1 316L Pipe Analysis

Material samples of 316L from the GENIV RCBC loop were obtained from 3" diameter, schedule 160 piping that had been replaced. The various samples had accumulated approximately 200 hours of operation at temperatures ranging between 20°C and 500°C. The CO2 fluid states were "subcritical gas" and "supercritical".

This analysis showed that the in-service pipe contained evidence of intergranular attack along the grain boundaries and pitting on the grain surfaces, as shown in Figure 9. These conditions were identified using a low-energy Backscatter Electron Imaging (BEI) SEM. There was a noticeable deposit in the intergranular trenches. Upon further analysis with EDS, the material was concluded to be carbonaceous. These results raised concerns that S-CO2 may be influencing the apparent materials degradation observed. Additional preventive maintenance pipe samplings were planned to gain further insight into these data.

In early May 2013, the Brayton team decided to obtain a sample from the GEN IV S-CO2 RCBC loop. It was determined that the leg that had the highest temperature should represent the conditions where corrosion would be the most severe in the loop. The sample was taken from the heater outlet indicated by the red circle in **Figure 10** (a). The sample was cut using a low-speed reciprocating saw to avoid sample contamination from cutting oils. Cross-sectional microscopy was used to gauge the depth of the affected base material to quantify the depth of the intergranular attack initially found in fresh pipe. **Figure 10** (b) shows the physical location of the sample taken from the loop; the actual sample is shown in **Figure 10** (c).

It was apparent that the inside diameter of the pipe exhibited uniform intergranular attack to a depth of $15\mu m \pm 4\mu m$. When analyzing the sample at 500x, small amounts of surface scale on the inside diameters (IDs) of the pipe were noticeable, presumably arising from operational corrosion. Scale was not uniform, and only presented itself in small amounts on the IDs of the pipe, which indicated that corrosion was insignificant over the range of conditions and durations that the 316L was exposed to during system operation. Furthermore, the scale was not found in the intergranular trenches, but only on the surface, as shown in **Figure 11**.

Observations during the piping analysis raised questions regarding the as-received material quality and the specifications obtained for the 316L piping. The original GEN IV piping is thought to be of lesser quality than domestic US piping material and, possibly, a counterfeit material. Details about the source of the piping and the level of manufacturing quality control are still uncertain. A pre-exposed material sample to establish a baseline was not secured, despite repeated requests to the manufacturer. Despite this lack of baseline data, it is thought that the "pickling" process, used to remove surface scales during manufacturing, resulted in the grain boundary trenching.

Pickling of stainless steels is a multi-step process that must be done after alloys are hot-worked to remove oxide scales that develop on the surface. Due to their high chromium content,

stainless steels typically develop adherent, robust chromium oxide scales, which are difficult to remove. Pickle liquors for stainless steels are, therefore, required to utilize a variety of acid mixtures that typically contain various concentrations or mixtures of three acids: sulfuric, nitric, and hydrofluoric [31]. Lack of control during pickling can result in pitting and an increase in surface roughness. Hydrofluoric acid has been shown to induce significant intergranular attack and pitting on 304SS, which is compositionally similar to 316SS, in only 42 seconds [6]. SNL has currently benchmarked all newly installed SS 316L pipes in the RCBC loop to keep track of the number of hours in service, and will continue periodic materials sampling. This sampling will provide information for material requirements and pipe quality standards related to S-CO2 systems. A mass spectrometer (Pfeiffer Vacuum Omni-Star) was installed downstream of the heater discharge and the turbine inlet to actively monitor the relative elemental compositions of materials being transported throughout the loop. These tests were initially benchmarked, and the details of these tests will be presented.

3.2 Turbine Erosion

During the rebuild of the turbomachinery, it was noticed that the turbine wheel and nozzles showed significant erosion, which was thought to be due to particulate matter in the flow stream. The turbomachinery continued operation for five months, until it was removed to undergo analyses that included microscopy, SEM, and EDS. **Figure 12** shows the substantial amount of erosion on the turbine nozzle and turbine. Another area of high-velocity flow is the compressor discharge. Inspection of these components revealed an absence of erosion, as shown in **Figure 13**. It is very important to note that where two-phase flow conditions exist, such as in the compressor, there have been no visible signs of erosion.

Turbine analysis was accomplished using microscopy and SEM/EDS. The results from microscopy showed substantial amounts of erosion. In addition, the inlet of the turbine wheel showed erosion that was apparently purely mechanical, resulting from particulate erosion, as seen in **Figure 14**. The reasoning behind the assumption of mechanically caused erosion is the fact that the turbine operates with high temperatures that are far in excess of the critical temperature, precluding the possibility of two-phase conditions that might lead to liquid impingement. Furthermore, erosion occurred primarily on the suction side of the blade.

Results from the SEM showed a different microstructure than what had been expected. (See **Figure 15**.) There are indications of plastic deformation from abrasion, potentially due to a plastically deformed layer of some metal. To accurately identify the material causing the abrasion, the material composition of C-22 (the material from which the turbine was constructed) was researched and compared to the EDS measurement, as shown in **Table 1**. There was a high amount of Fe present on the surface of the turbine. The current best hypothesis is that small shavings of ferritic steel may be the cause of the erosion.

3.3 Nozzle Erosion

Erosion has been present in the S-CO2 Brayton loop at least since 2010. Mechanical abrasion has been noted on both the nozzles and the turbines. Initially, it was thought that the erosion was a temporary problem associated with the fabrication of the loop, but the erosion did not stop or lessen in severity. There also was concern that erosion might be present in the high-temperature heat exchanger, because of the erosion that had been happening in the turbine nozzle. Due to the proprietary nature of Heatric PCHEs, it is not possible to cut open the heat exchangers; therefore, a similar candidate, the turbine nozzle, was selected to undergo the same analysis.

Advanced microscopy was selected as the way to visually examine the nozzle. This examination noted particulate erosion, much like that associated with the turbine, but with a more aggressive behavior. Once this particulate erosion was identified, EDS analysis was performed to try to understand its origin and nature.

Visual inspection of the sample showed extreme wastage. **Figure 16** shows a channel eroded out of the nozzle that equals the height of the inlet of the turbine vane.

Following these initial observations, the nozzle was analyzed using EDS on the undercut of the nozzle. Because time would not permit sectioning the nozzle with a cutting technique, a similar location was chosen for analysis. (See **Figure 16**.) The EDS analysis showed that there was significant iron enrichment present on the surface, as well as a decrease in surficial Ni. As shown in **Table 2**, the iron content was 40.7 by percent, which was significantly higher than the expected 23.8 percent.

3.4 Discussion of Particulate Source

During the tests, a scavenging pump removed CO2 from the TACs, due to seal leakage, to minimize windage losses. CO2 was then input into a series of carbon steel tanks that served two purposes: an inventory tank, and a flow-directing pathway (**Figure 17**). Currently, it is believed that the iron oxide came from these tanks.

The tanks were hydro-pressure tested to ensure their compliance with safety requirements, which resulted in some rust formation within the tank. Because one of the tank's dual purposes was to serve as a flow turbulator, any spallation of the iron oxide could be readily injected into the RCBC, potentially causing the damage observed in the turbine and nozzles. Plumbing changes were made to only utilize the tanks as inventory storage, as shown in **Figure 17**. The inventory tanks were moved from within the loop to an isolated section of the loop. This configuration change was made for multiple reasons. First, this change reduced the total volume of CO2 needed to fill the loop, as the storage tanks will be isolated from the loop with a valve. CO2 will only move one direction, from the loop into the inventory tanks, to 1) reduce CO2 volume in the loop during the test, and 2) to minimize the possibility of contaminants flowing into the loop. In the original configuration, the storage tanks were part of the loop, and CO2 flowed through them during testing.

As the system is heated, thereby decreasing the CO2 density within the system, the inventory tank is used to control the resulting expansion. Nonetheless, while spallation was not due to components or flow piping, this raises a concern in regards to erosion effects if any spallation occurs in a pilot-plant setting.

Currently, the 125kW-rated turbine will approach several hundred meters per second at max tip velocities. As the system is scaled up in size to 5MW or to 10MW, this speed will remain relatively constant or may increase by 24%. This emphasizes the need for rigorously developing methodologies to protect the turbomachinery from particulates that will damage components, and acutely shorten component lifetime. Periodic maintenance practices, such as pigging and fluid chemistry control, will be critical to ensure reasonable lifetimes for the major components, in addition to determining the best materials and strength-resistant coatings.

3.5 Conclusion and Path Forward

Sandia National Laboratories is currently investigating erosion mechanisms in the recompression closed Brayton cycle. It was found that there is currently an absence of corrosion in the S-CO2 cycle components. The initial speculation of the intergranular attack was suspected to be corrosion, but, after careful consideration, it was found that the intergranular attack was caused by the ASTM 312 and 376 processes, in which the pipe was pickle passivated to remove any surface scale that had formed during the fabrication of the pipe. Testing will continue to look for signs of intergranular corrosion in this piping, using well-documented (hours of operation) 316L schedule 160 pipe samples.

After investigating the erosion samples from the turbine and turbine nozzle, a stronger level of effort will be placed on the identification of the source of this damage. Currently, it is thought that the erosion is caused by iron particulates, which are believed to come either from the machining of loop components or from the mild steel inventory tanks. The investigation is not limited to these sources, but it has been determined that the erosion particles are high in iron content.

Several general strategies are being employed to respond to erosion in S-CO2 power cycles. This includes the installation of an *in situ* Thermostar mass spectrometer to identify loop contaminates. In addition, erosion-resistant materials and coatings for use on the turbines and turbine nozzles associated with these prototype systems are being investigated.

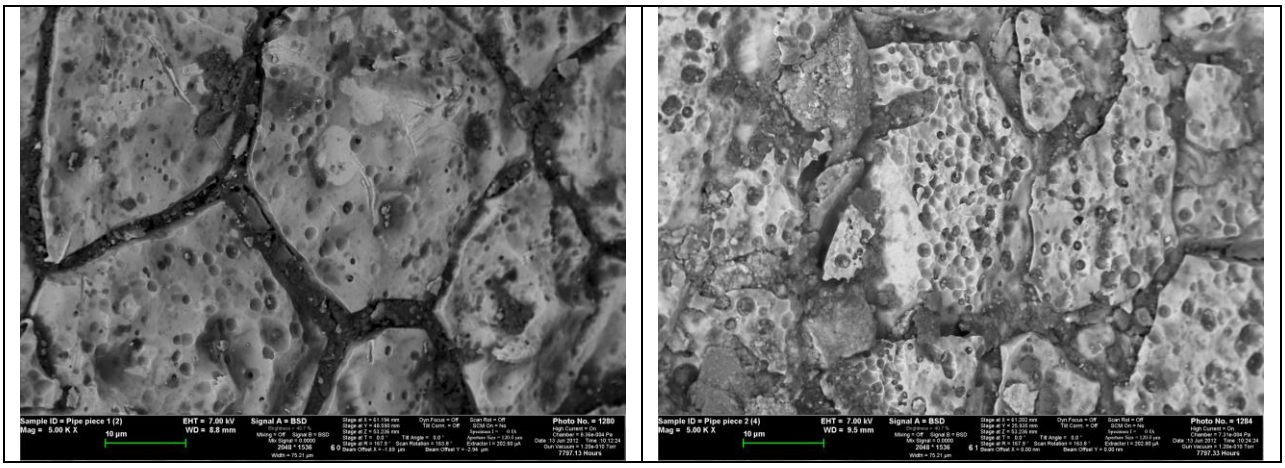

Figure 9: Two SEM images of the in-service SS 316L piping showing significant intergranular corrosion and pitting.

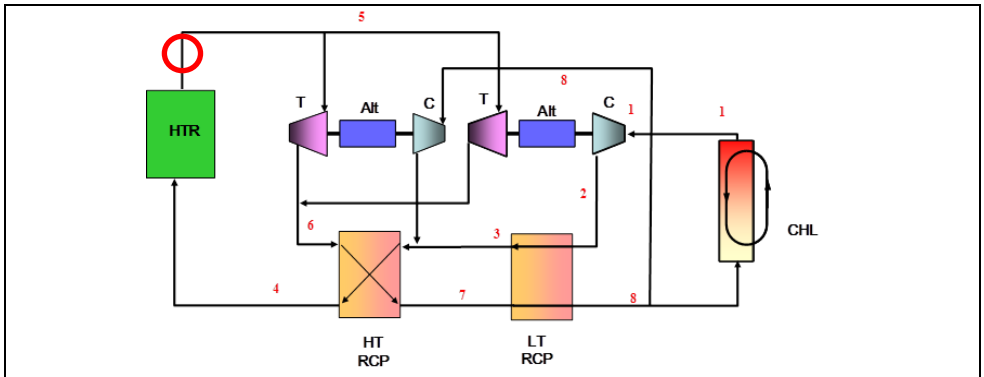

10A

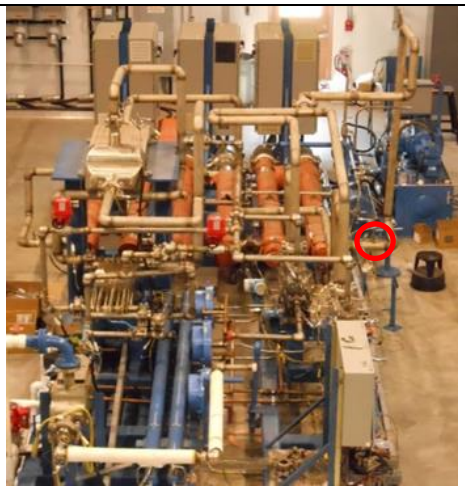

10B

10C

Figure 10: Sample location in schematic view (red circle) (a). Sample location is within physical view (red circle) (b). Corrosion sample removed (c).

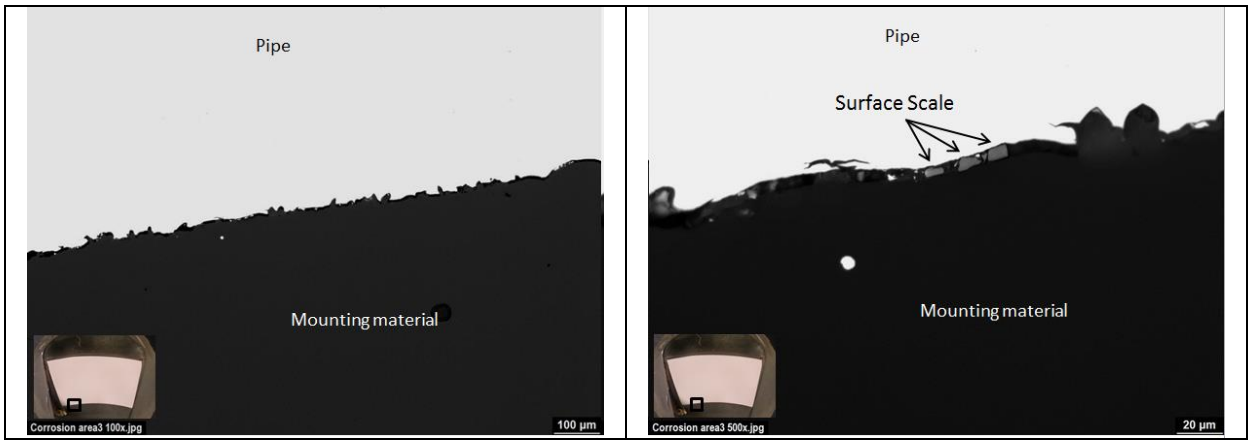

Figure 11: 100x (left) and 500x (right) images indicate surface features indicative of intergranular attack. Some surface scale was observed, and will be identified using electron spectroscopy techniques.

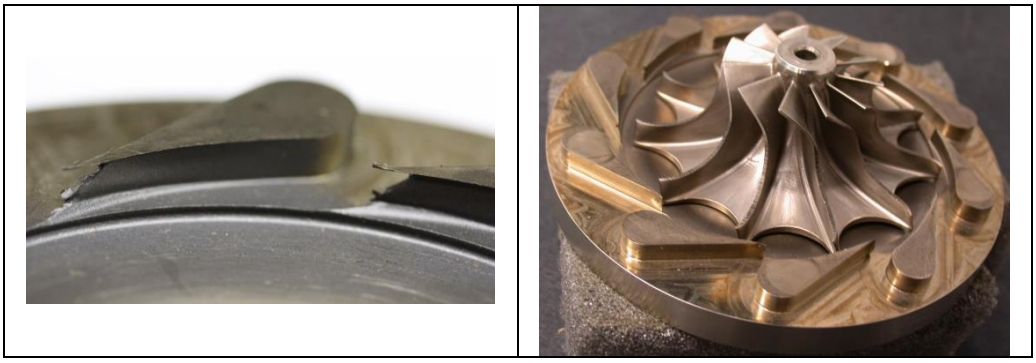

Figure 12: Turbine nozzle (left) with substantial amount of erosion, and turbine wheel (right) with placement inside turbine nozzle.

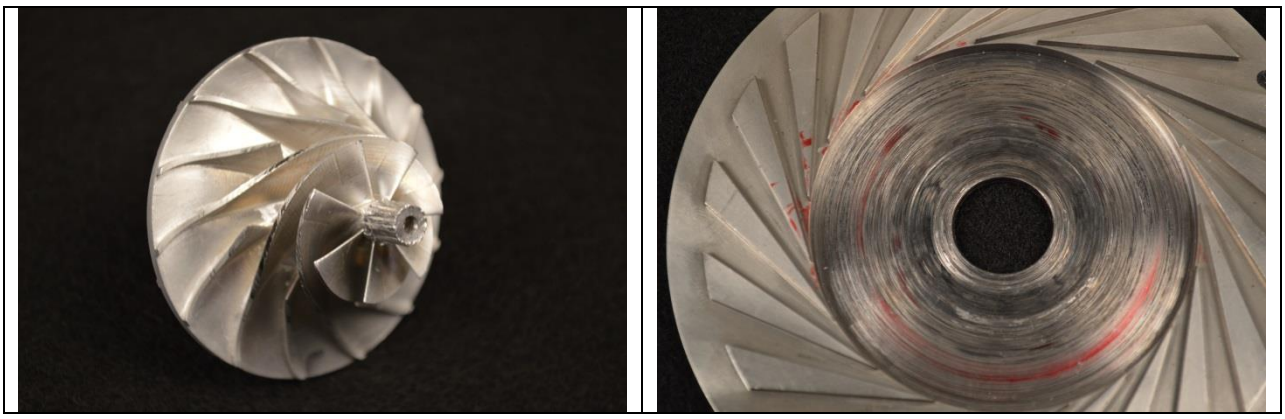

Figure 13: Compressor (left) and compressor diffuser (right) showing no signs of erosion.

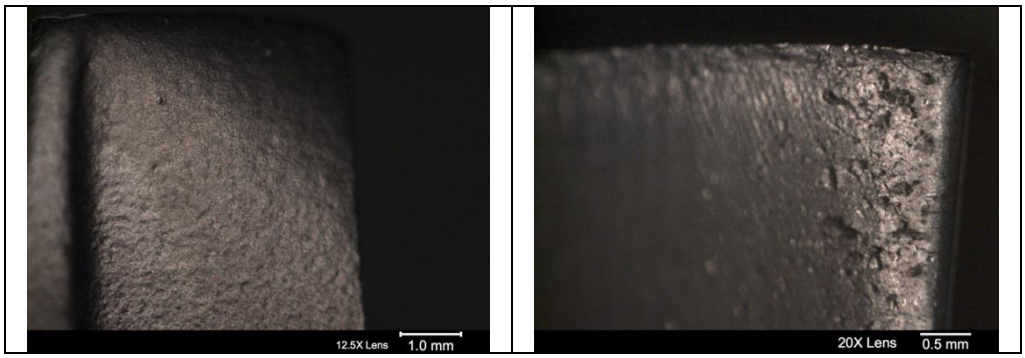

Figure 14: Erosion on the Turbine (L); particulate erosion on turbine blade (R).

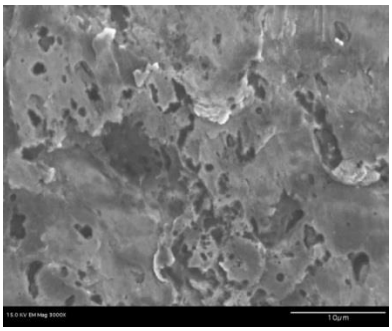

Figure 15: SEM showing different microstructure.

Figure 16: Turbine Nozzle with undercut; EDS sample location identified.

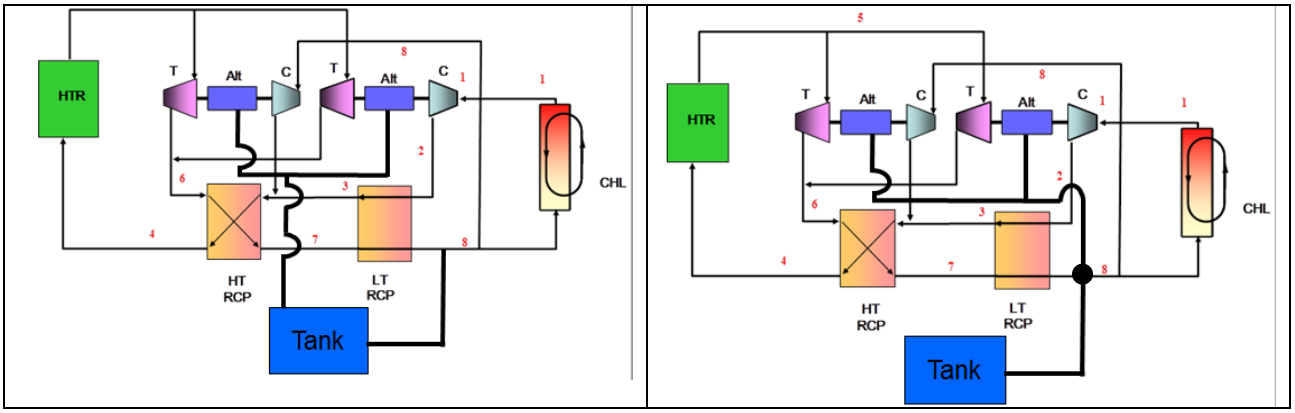

Figure 17: Layout during test (left) and modified layout after erosion (right).

Tables

Table 1: EDS comparison: IN C-22 vs. actual on turbine wheel

	C	Si	V	Mn	Cr	Fe	Ni**	Mo	Co	W
C-22	0.010*	0.08*	0.35*	0.50*	22	3	56	13	2.5*	3
EDS Data					19.8	11.6	56.9	9.2		2.1
***max, **balance**										

Table 2: EDS comparison: IN 718 vs. actual on turbine nozzle

	C	Si	V	Mn	Cr	Fe**	Ni	Mo	Co	Ti	Nb+Ta
In718	0.008*	0.35	0.8*	0.35*	21*	23.8	55*	3.3	1.0*	3	5.50*
EDS Data					19	40.7	35.8	3.1			
***max, **balance**											

References

1. Moore, R.C. and T.M. Conboy, *Metal corrosion in a supercritical carbon dioxide - liquid sodium power cycle*, 2012, SAND2012-0184, Sandia National Laboratories, Albuquerque N. M.
2. Rouillard, F., F. Charten, and G. Moine, *Corrosion behavior of different metallic materials in supercritical carbon dioxide at 550C and 250 bars.* Corrosion, 2011. **67**(9).
3. Kruizenga, A.M., D.D. Gill, and M. LaFord, *Materials Corrosion of High Temperature Alloys Immersed in 600°C Binary Nitrate Salt*, 2013, SAND2013-2526, Sandia National Laboratories, Livermore C.A.
4. Kruizenga, A.M., *Corrosion mechanisms in chloride and carbonate salts*, 2012, SAND2012-7594, Sandia National Laboratories, Livermore C. A.
5. Bradshaw, R.W., *Oxidation and Chromium Depletion of Alloy 800 and 316SS by Molten NaNO3-KNO3 at Temperatures Above 600 Degrees Centigrade*, 1987, SAND86-9009, Sandia National Laboratories, Livermore C. A.
6. Ambrosek, J., *Molten Chloride Salts for Heat Transfer in Nuclear Systems*, in *Nuclear Engineering and Engineering Physics*2011, University of Wisconsin-Madison: Madison, Wisconsin. p. 254.
7. Olson, L., *Materials Corrosion in Molten LiF-NaF-KF Eutectic Salt*, in *Nuclear Engineering*2009, University of Wisconsin-Madison: Madison, Wisconsin. p. 281.
8. Ludwig, D., et al., *High temperature electrochemistry of molten fluoride salt for measurement of dissolved chromium.* Corrosion Engineering Science and Technology, 2011. **46**(4): p. 360-364.
9. Dostal, V., M.J. Driscoll, and P. Hejzlar, *A Supercritical Carbon Dioxide Cycle for Next Generation Nuclear Reactors*, 2004.
10. Dostal, V., et al., *Medium-power lead-alloy fast reactor balance-of-plant options.* Nuclear Technology, 2004. **147**(3): p. 388-405.
11. Iverson, B.D., et al., *Supercritical CO2 Brayton cycles for solar-thermal energy.* Applied Energy, 2013. **111**: p. 957-970.
12. Le Moullec, Y., *Conceptual study of a high efficiency coal-fired power plant with CO2 capture using a supercritical CO2 Brayton cycle.* Energy, 2013. **49**(1): p. 32-46.
13. Ellis, B.N., *On insulation resistance.* Circuit World, 1995. **21**(2): p. 5-11.
14. Siegel, N.P., *Thermal energy storage for solar power production.* Wiley Interdisciplinary Reviews: Energy and Environment, 2012. **1**(2): p. 119-131.
15. McKinnon, D.L. *Insulation resistance profile (IRP) and its use for assessing insulation systems*. in *2010 IEEE International Symposium on Electrical Insulation, ISEI 2010, June 6, 2010 - June 9, 2010*. 2010. San Diego, CA, United states: Institute of Electrical and Electronics Engineers Inc.
16. Kruizenga, A.M., et al., *Supercritical carbon dioxide heat transfer in horizontal semicircular channels.* Journal of Heat Transfer, 2012. **134**(8).
17. Momozaki, Y., et al., *Experimental investigations on sodium plugging in narrow flow channels.* Nuclear Technology, 2010. **171**(2): p. 153-160.

18. Southall, D., R. Le Pierres, and S.J. Dewson. *Design considerations for compact heat exchangers*. in *International Conference on Advances in Nuclear Power Plants, ICAPP 2008, June 8, 2008 - June 12, 2008*. 2008. Anaheim, CA, United states: American Nuclear Society.
19. Lai, G.Y., *High Temperature Corrosion of Engineering Alloys*. 1990: ASM International.
20. de Waard, C. and D.E. Williams, *Predication Of Carbonic Acid Corrosion In Natural Gas Pipelines.* Industrial Finishing and Surface Coatings, 1976. **28**(340): p. 24-26, 28.
21. Zhang, Y., et al., *Discussion of the CO2 corrosion mechanism between low partial pressure and supercritical condition.* Corrosion Science, 2012. **59**(0): p. 186-197.
22. Rouillard, F., et al., *CORROSION BEHAVIOR OF DIFFERENT METALLIC MATERIALS IN SUPERCRITICAL CO_2 550°C AND 250 BARS*, in *CORROSION 2010*2010, NACE International: San Antonio, TX.
23. Tan, L., et al., *Corrosion of austenitic and ferritic-martensitic steels exposed to supercritical carbon dioxide.* Corrosion Science, 2011. **53**(10): p. 3273-3280.
24. Rouillard, F., et al., *Corrosion of 9Cr Steel in CO2 at Intermediate Temperature I: Mechanism of Void-Induced Duplex Oxide Formation.* Oxidation of Metals, 2012. **77**(1-2): p. 27-55.
25. Cao, G., et al., *Corrosion of austenitic alloys in high temperature supercritical carbon dioxide.* Corrosion Science, 2012. **60**(0): p. 246-255.
26. Firouzdor, V., et al., *Corrosion of a stainless steel and nickel-based alloys in high temperature supercritical carbon dioxide environment.* Corrosion Science, 2013. **69**: p. 281-291.
27. Rouillard, F., et al., *Corrosion of 9Cr Steel in CO2 at Intermediate Temperature II: Mechanism of Carburization.* Oxidation of Metals, 2012. **77**(1-2): p. 57-70.
28. Elthalabawy, W. and T.I. Khan. *Diffusion bonding of austenitic stainless steel 316L to a magnesium alloy*. in *11th International Symposium on Advanced Materials, ISAM-2009, August 8, 2009 - August 12, 2009*. 2010. Islamabad, Pakistan: Trans Tech Publications Ltd.
29. Guo, H., E. Steinhauer, and J.J. Chene, *Solid state diffusion bonding for structural joining with similar and dissimilar materials.* Welding in the World, Le Soudage Dans Le Monde, 1996. **37**(3): p. 107-113.
30. Outotec, *HSC Chemistry 7*, 2013.
31. *Metals Handbook Desk Edition*, J.R. Davis, Editor 2013, ASM International.

Electronic Distribution:

1 Argonne National Laboratory
Robert Hill
9700 South Cass Avenue, Bldg. 208
Argonne, IL 60439-4842
(electronic copy) bobhill@anl.gov

1 Office of Nuclear Energy
Steven Reeves
19901 Germantown Road, D-424
Germantown, MD 20874
(electronic copy) Steven.Reeves@Nuclear.Energy.gov

1 Office of Nuclear Energy
Brian Robinson
19901 Germantown Road, D-421
Germantown, MD 20874
(electronic copy) Brian.Robinson@Nuclear.Energy.gov

1 MS1136 Gary Rochau, 6221 (electronic copy) gerocha@sandia.gov

1 MS1136 James Pasch, 6221 (electronic copy) jjpasch@sandia.gov

1 MS0899 Technical Library, 9536 (electronic copy)

THIS PAGE INTENTIONALLY LEFT BLANK


Sandia National Laboratories